Supporting Information for

Lanthanum-based Double Perovskite Nanoscale Motifs as Support Media for the Methanol Oxidation Reaction

Scott C. McGuire[1], Christopher Koenigsmann[2], Chun Chieh Chou[1], Xiao Tong[3], and Stanislaus S. Wong[1,*]

Email: stanislaus.wong@stonybrook.edu

[1]Department of Chemistry, State University of New York at Stony Brook,
Stony Brook, NY 11794-3400

[2]Department of Chemistry, Fordham University, Bronx, NY 10458

[3]Center for Functional Nanomaterials, Building 735,
Brookhaven National Laboratory, Upton, NY 11973

I. Experimental Section

Materials: All materials were used, as purchased. Specifically, we utilized lanthanum nitrate hexahydrate (99.9%, Alfa Aesar), nickel nitrate hexahydrate (98%, Alfa Aesar), manganese nitrate tetrahydrate (98%, Alfa Aesar), manganese acetate tetrahydrate (99.99%, Aldrich), ammonium hydroxide (28-30 wt% NH_3 in water, Acros Organics), sodium hydroxide (98.5%, Acros Organics), potassium hydroxide (Fisher Scientific), lithium hydroxide monohydrate (56%, Acros Organics), dihydrogen hexachloroplatinate(IV) hydrate (H_2PtCl_6, 99.9%, Alfa Aesar), sodium borohydride ($NaBH_4$, 99.99%, Alfa Aesar), ethanol (denatured, BeanTown Chemical), polyvinylpyrrolidone (PVP, M.W. = 40,000, Alfa Aesar), and glycine (99+%, Alfa Aesar).

Synthesis of La_2NiMnO_6 (LNMO) nanocubes (NCs): In a characteristic synthesis of LNMO nanocubes, 1 mmol of $La(NO_3)_3$, 0.5 mmol of $Mn(NO_3)_2$, 0.5 mmol of $Ni(NO_3)_2$, 7 mmol of glycine (i.e., functional role of surfactant), and 300 mg of PVP (polyvinyl pyrrolidone) (MW = 40,000) (i.e., functional role of surfactant) were dissolved in 25 mL of water. Next, the pH of the solution was adjusted to the desired pH of 8.9 by slowly adding in NH_4OH. The solution was then transferred to a Teflon-lined stainless-steel autoclave and heated at 180 °C for 12 h. The resulting product was collected after a centrifugation step, washing with water and ethanol, and finally oven drying. The product was then annealed at 600°C for 2 h, using a ramp rate of 5 °C/min. The annealed product was subsequently dispersed in 0.2 M acetic acid, sonicated for 1 h, centrifuged, and ultimately washed with water and ethanol in order to remove any excess acid. The sizes of the LNMO NCs could be reliably controlled by adjusting the pH of the solution, prior to the hydrothermal reaction. Herein, we use the notation of LNMO-n, wherein the designation of ‘n’ is the pH used in the reaction process. Hence, as an example, LNMO-8.9 refers to LNMO synthesized at a pH of 8.9.

Synthesis of $LaNiO_3$ (LNO) nanocubes (NCs): In a typical synthesis, 1 mmol of $La(NO_3)_3$, 1 mmol of $Ni(NO_3)_2$, 3 mmol of glycine, and 300 mg of PVP (MW = 40,000) were dissolved in 25 mL of water. Next, for optimal results, the pH was adjusted to 7.4 by slowly adding in NH_4OH. The solution was then transferred to a Teflon-lined stainless-steel autoclave and heated at 180°C for 12 h. The rest of the procedure was identical to that used to produce LNMO nanocubes, except that the LNO NCs were washed with a weaker acid solution, i.e. 0.01 M acetic acid, to prevent dissolution of this latter LNO control sample.

Synthesis of $LaMnO_3$ (LMO) nanocubes (NCs): In a representative synthesis, 1 mmol of $La(NO_3)_3$, 1 mmol of $Mn(NO_3)_2$, 8 mmol of glycine, and 300 mg of PVP (MW = 40,000) were dissolved in 25 mL of water. Next, to promote sample homogeneity and monodispersity, the pH of the solution was adjusted to 8.7 by slowly adding in NH_4OH. Otherwise, the rest of the protocol was the same as that previously utilized to generate LNMO nanocubes.

Synthesis of La_2NiMnO_6 (LNMO) nanorods (NRs): We utilize a modified two-step procedure which was initially reported for the synthesis of Y_2NiMnO_6 nanorods.[1] The (i) first step consisted of generating metal hydroxide composite nanowire intermediates followed by a (ii) second step, in which the intermediates were annealed, thereby forming the final perovskites. Specifically, the metal hydroxide intermediates were initially formed by dissolving 1.28 mmol $La(NO_3)_3$, 0.64 mmol $Ni(NO_3)_2$, and 0.64 mmol $Mn(acetate)_2$ in 20 mL of water, followed by slowly adding in a 5 mL aliquot of a 5 M NaOH solution and allowing the mixture to stir for 30 min. The solution was then transferred to a 25 mL Teflon liner until a ~80% capacity was achieved, and then it was sealed within a stainless-steel autoclave. The autoclave was heated at 200 °C for 24 h. The intermediates were subsequently washed with aliquots of water, acetone, and ethanol, and left to dry in an oven, overnight. The as-obtained intermediates were then annealed within a tube furnace at 800 °C. The annealed products were later dispersed in 0.2 M acetic acid, sonicated for 1 h, then collected by centrifugation, and finally washed several times with water and ethanol.

Deposition of Pt nanoparticles onto perovskite supports: Individual perovskite supports were dispersed in an aqueous solution of H_2PtCl_6, with a final perovskite concentration of 1 mg/mL, in order to achieve a mass loading of 50%. Next, an aqueous solution of $NaBH_4$ (16 mg/mL), created by using a volume of 1 mL of $NaBH_4$ solution per 2 mL of the perovskite dispersion, was added in, and the resulting mixture was allowed to stir for 30 min. The solution was subsequently centrifuged, and the resulting solid was washed with aliquots of water and ethanol for several times. The catalyst was then dispersed in ethanol with a final concentration of 2 mg of catalyst per 1 mL of ethanol.

Structural Characterization Techniques

Scanning electron microscopy: SEM characterization was used to examine the morphology of the as-prepared perovskites. Samples were dispersed in ethanol and subsequently drop cast onto a *p*-doped silicon substrate. SEM results were obtained using not only a Hitachi S-4800 SEM but also a JEOL 7600 field emission SEM instrument. Images were collected with an accelerating voltage of 5 – 10 kV. SEM-EDS results were obtained using a Zeiss LEO 1550 SEM instrument, equipped with a EDAX EDS detector, which was operated at an accelerating voltage of 20 kV.

Transmission electron microscopy: Complementary TEM characterization helped to identify the morphology of the as-prepared perovskites and their immobilized Pt catalysts. Samples were dispersed in ethanol and subsequently drop cast onto a lacey carbon-coated copper grid. Acquired images were obtained using a JEOL JEM-1400 TEM instrument, which not only was equipped with a 2048 × 2048 Gatan CCD camera system but also had been operating with an acceleration of 120 kV.

High resolution TEM: High resolution TEM (HRTEM) images and accompanying energy dispersive X-ray spectroscopy (EDS) data were obtained using a JEOL JEM-2100F microscope, operating with an acceleration voltage of 200 kV. In particular, EDS data and scanning transmission electron microscopy (STEM) images were taken using STEM mode. Relevant samples were prepared through their dispersal in ethanol, followed by drop-casting onto a lacey carbon-coated copper grid.

Powder X-ray diffraction: XRD patterns were measured as a means to confirm not only the chemical composition but also the crystallinity of as-prepared samples. Powder diffraction samples were generated by dispersing samples in ethanol, drop casting aliquots, and ultimately drying them onto zero-background holders. Powder X-ray diffraction (XRD) patterns were measured using a Rigaku MiniFlex diffractometer, operating in the Bragg-Brentano setup in the presence of Cu Kα radiation ($\lambda = 1.54$ Å). The diffraction patterns were all collected with a scanning rate of 20° min^{-1} in the range of 10° to 80°.

X-ray photoelectron spectroscopy: XPS was employed to acquire insights into the chemical composition of sample surfaces. Samples were prepared by dispersing the as-prepared perovskite powders in toluene and drop casting them onto silicon wafers, measuring 1 cm × 1 cm. The silicon wafers were placed into an ultrahigh vacuum chamber with a pressure of less than 5×10^{-9} Torr. XPS measurements were carried out using a home-built XPS surface analysis system, operating with a hemi-spherical electron energy analyzer (SPECS, XR50). Al Kα (1486.61 eV) source radiation was supplied using current-voltage conditions of 13 kV and 30 mA, respectively. An angle of 45° was set between the analyzer and the X-ray sources, with the photoelectrons being collected along the sample's surface normal vector. Acquired data were analyzed, fitted, and interpreted using the commercial CasaXPS software. The positions of the peaks were corrected by using a carbon standard set at 284.8 eV.

BET analysis: The surface areas of the perovskite samples were analyzed using a Quantachrome Nova 2200e surface area analyzer. The samples were first evacuated at room temperature and then were heated to 250°C for 2 h. The surface area was calculated from a linear 5-point BET plot, acquired from analysis at 77 K using N_2 adsorbate gas.

Electrochemical characterization: The as-prepared catalysts were drop cast onto a glassy carbon rotating disk electrode (Pine Research, 5.0 mm). First, the electrode was polished using an aluminum oxide slurry. The catalysts were dispersed in ethanol with a concentration of 2 mg mL^{-1} and then immobilized onto the electrode by adding in two 5 μL drops onto its surface. After drying in air, the electrode surface was then sealed using one 5 μL drop of a 0.025% Nafion solution in ethanol. The catalyst-loaded electrode was subsequently immersed in water to get rid of any impurities, prior to any electrochemical measurements.

Electrochemical data were acquired in 0.1 M perchloric acid (Fisher Scientific, optima grade) solutions, which were prepared using high-purity water with a resistivity value of 18.2 MΩ cm. Prior to taking these measurements, Ar gas was bubbled in, such that the solutions were saturated with this inert gas to remove any dissolved oxygen. Platinum wire was used as the counter electrode, while an Ag/AgCl combination (4.0 M KCl with Ag) was used as the reference electrode. All of the potentials are reported with respect to the reversible hydrogen electrode (RHE). The electrochemical properties of our as-generated catalysts were investigated using cyclic voltammetry (CV). CVs were obtained using a scan rate of 20 mV s^{-1} in deoxygenated 0.1 M perchloric acid. Moreover, the electrochemically active surface area

(ECSA) was determined by using the integrated hydrogen adsorption (H_{ads}) area within the CV analysis, using 210 μC cm^{-2} as the conversion factor.

MOR kinetics were assessed using an Ar-saturated solution incorporating 0.5 M methanol (Fisher Scientific, Optima grade) within a 0.1 M $HClO_4$ electrolyte. Linear sweep voltammetry (LSV) data for the methanol oxidation reaction were collected using a scan rate of 20 mV s^{-1}. Either the observed current was recorded at 0.80 V in the onset region or the LSV peak was normalized to the Pt ECSA in order to provide for a specific activity reading. The activity of Pt supported onto the perovskite particles was compared with that of a commercial carbon-supported Pt nanoparticle catalyst sample (TKK TEC10E50E).

II. Additional Discussion:

A. Summary of Glycine Findings

To summarize, LNMO NCs begin to form at ~6 mmol of glycine with the size of the as-generated NCs rising with ever increasing amounts of glycine. This observable and reproducible augmentation in particle size is likely influenced by three main factors. *First*, as the amount of glycine increases, complexation between the metal ions and glycine also correspondingly proliferates, a scenario which favors NC growth. *Second*, when the concentration of glycine exceeds that of the metal ions, the likelihood of glycine polymerization may increase,[2] which could also favor an expansion in the size of the resulting NCs, due to metal ion coordination with the larger glycine polymeric species. As such, the precise quantity of glycine introduced into the reaction medium is undeniably crucial to perovskite nanocube synthesis; higher incorporated amounts of glycine generally yield larger and purer particles. Nevertheless, an excess of glycine may result in competing polymerization processes, which may lead to a higher degree of polydispersity, which represents a less desirable outcome. *Third*, our experiments imply that a certain minimum 'threshold' level of glycine is likely needed during the annealing step to act as a 'fuel' to facilitate formation of the desired perovskite.

B. Effect of pH on the synthesis of perovskite nanocubes:

The synthesis of LMO and LNMO NCs of similar sizes apparently requires a higher pH as compared with LNO. We can potentially ascribe these observations to the comparatively lower stability of Mn-glycine complexes as compared with the analogous Ni-glycine complex. In addition, the influence of pH on the formation of the perovskite NCs can likely be further explained by changes within the chemical bonding structure of glycine, at different pH values. Solid glycine exists in its zwitterionic form ($^{+}H_3N\text{-}CH_2\text{-}COO^{-}$), wherein the amino group is positively charged and the carboxylic acid group is negatively charged. In aqueous media, the zwitterion is favored at its isoelectric point (pH = 5.97).[3] Upon further increasing the pH, the concentration of the negatively charged species of glycine correspondingly rises. The pK_2 value of glycine is known to occur at 9.6, which is where there are equal concentrations of the negatively charged and neutral species.[4] As such, in order to sufficiently complex Mn with glycine, a higher amount of the negatively charged glycine may be necessary as compared with Ni. Indeed, this assertion is logical, especially when considering that Ni ($\chi = 1.91$) is more electronegative than Mn ($\chi = 1.55$)[5] and as such, would coordinate onto glycine with greater ease. One consequence is that a higher concentration of the negatively charged glycine species, which would be present under higher pH conditions, would therefore be needed to enable the less electronegative Mn to form equivalent amounts (as compared with Ni) of this key precursor metal-glycine complex. Such behavior is consistent with experimental observations.

C. Effect of various reaction parameters on the synthesis of LNMO nanorods:

To test the role of (a) solvent, we switched the reaction medium to ethanol. Specifically, exchanging water with ethanol was expected to increase the diameters of the nanowires, because in a previous report on the synthesis of $La(OH)_3$ nanowires, it was found that decreasing the water/ethanol ratio did in fact significantly boost the observed diameters.[6] However, herein, the expected increase in diameter was not in fact noted. Rather, there was (i) a significant decrease in the length of nanorods, (ii) a rise in sample polydispersity, (iii) the production of minor $LaMn_2O_5$ impurities coupled with (iv) the formation of octagonal nanoplatelets, as shown in Figure S10A. Increasing the (b) reaction time from 24 to 48 h had little to no obvious impact upon the morphology of the intermediates. Similarly, (c) either adding in KCl or using $KMnO_4$ as the Mn source led to little if any perceptible effect on the morphology of the final product. Interestingly, we were able to isolate intermediate nanowires, measuring ~30 nm in diameter, as highlighted in Figures S10B-C.

Preliminary results in terms of decreasing the (d) hydrothermal reaction temperature from 200 to 150°C suggested that lowering this temperature could decrease the average diameters of the intermediates and the resulting products from ~40 nm to a range of 20 to 30 nm, as illustrated in Figure S10D. This result would seem to suggest that the reaction temperature can indeed influence the resulting morphology, a finding consistent with prior reports of similar systems, which demonstrate that increasing the reaction temperature can indeed slightly increase the nanorod / nanowire diameter.[7] However, our experiments also support the idea that such a change in size is neither sufficiently striking nor remarkable. In particular, given the safety limitations of our autoclave with its maximum feasible operating temperature of no more than 240°C, it is highly unlikely that we can merely toggle reaction temperature to achieve a perceptibly greater dimension comparable to that of our synthesized nanocubes (i.e., ~200 nm).

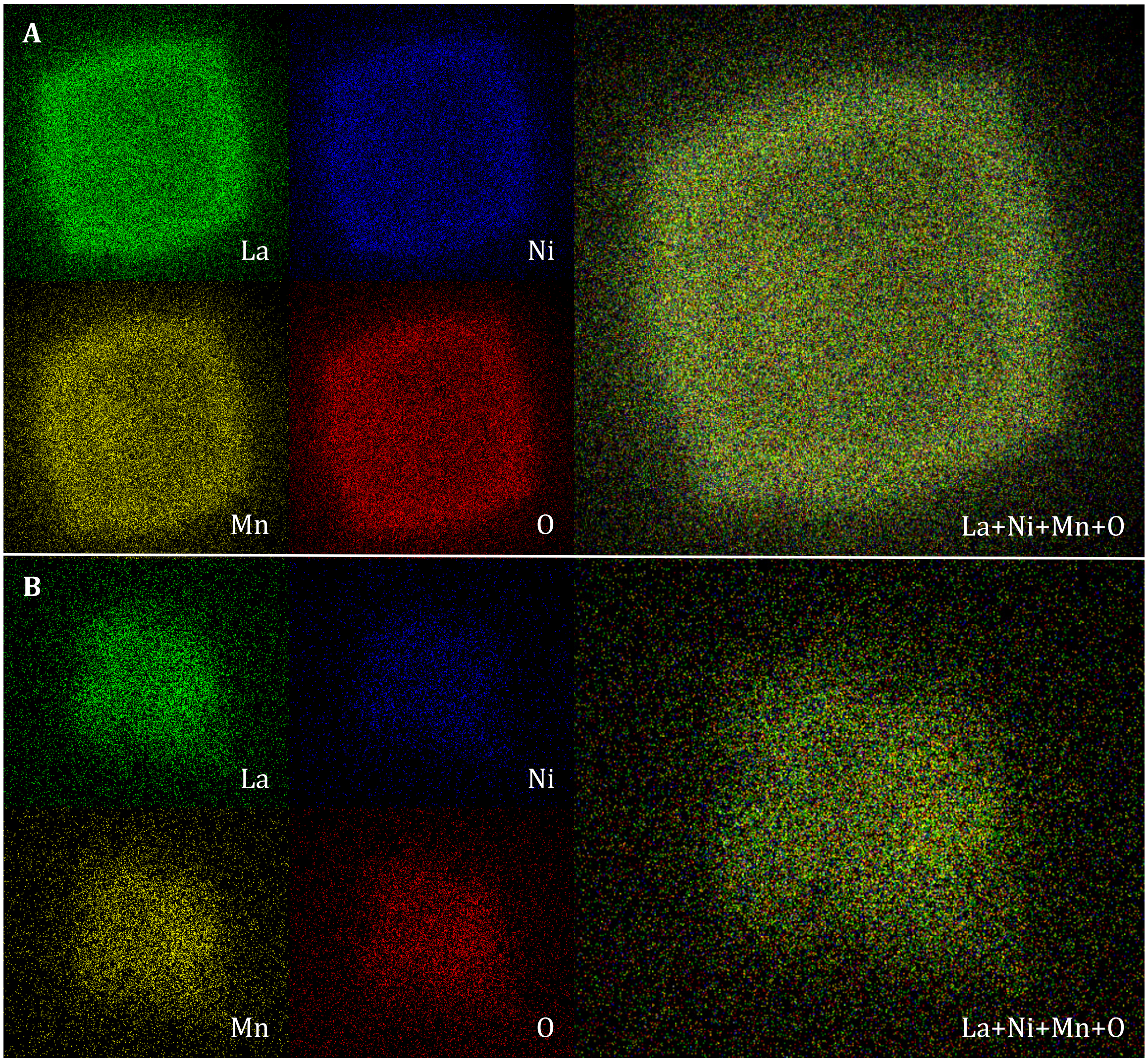

Figure S1. EDS mapping images of (A) LNMO-8.7 NCs and (B) LNMO-9.3 NCs, respectively.

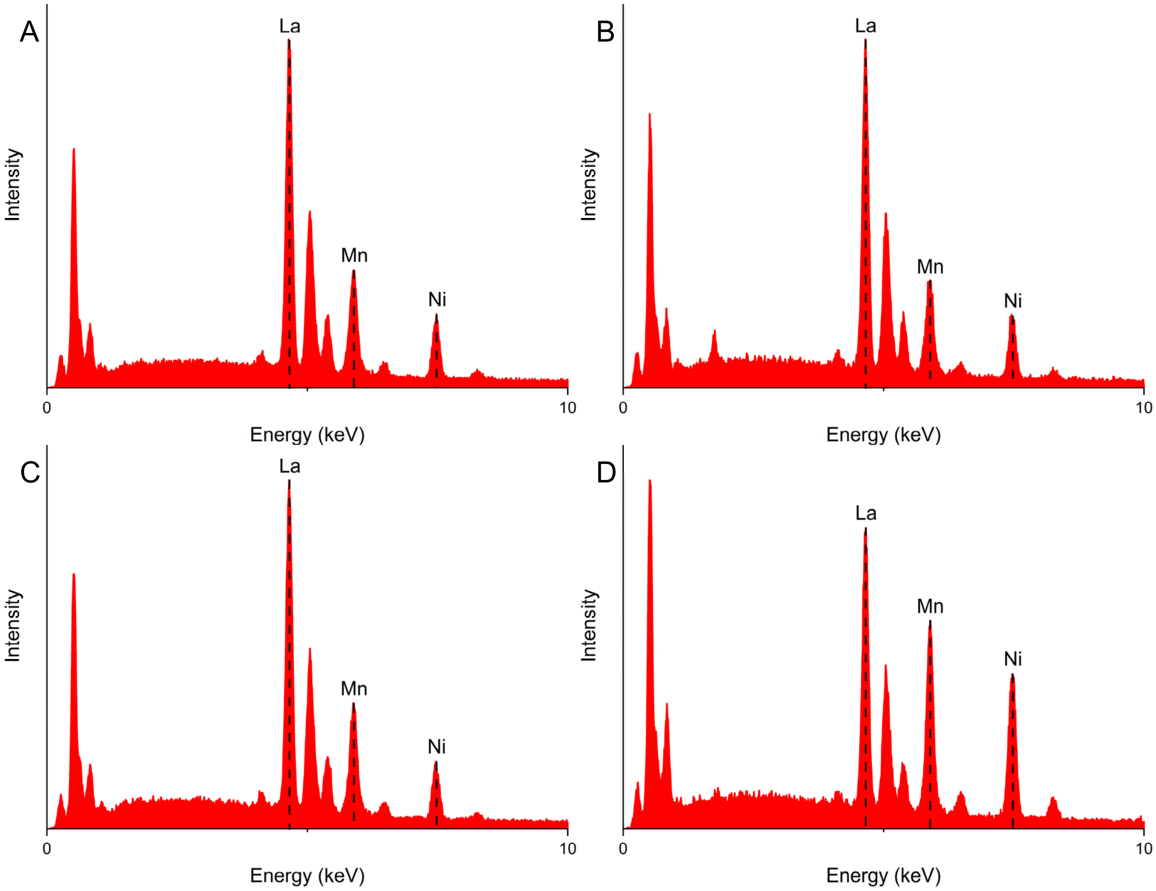

Figure S2. EDS spectra for (A) LNMO-8.7 NCs, (B) LNMO-8.9 NCs, (C) LNMO-9.3 NCs, and (D) LNMO NRs, respectively.

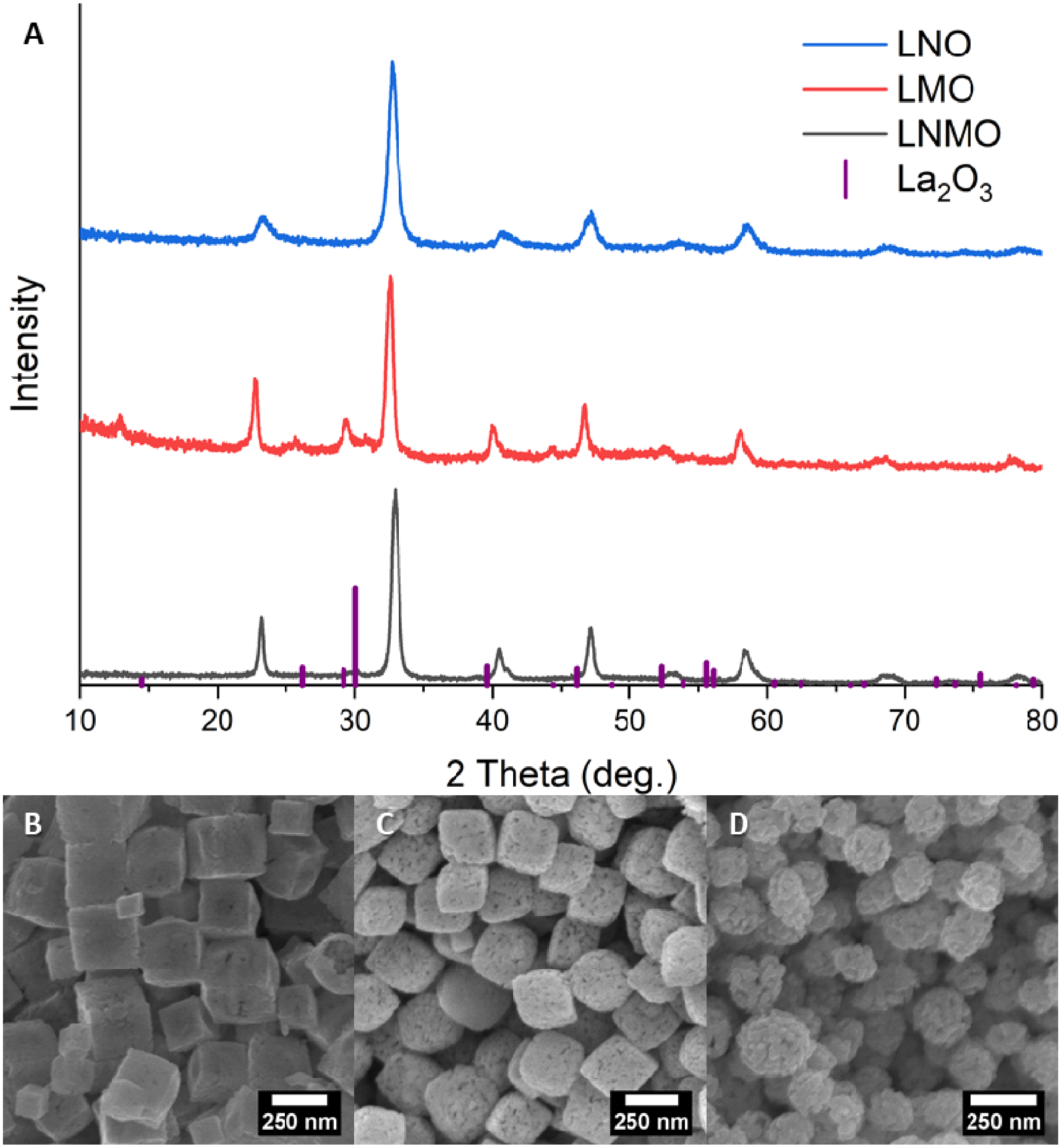

Figure S3. (A) XRD patterns of LNO (blue curve), LMO (red curve), and LNMO NCs (black curve) without any acetic acid washing. The reference pattern for La_2O_3 is shown by the purple line.[8] SEM images of (B) LNMO-8.9, (C) LMO, and (D) LNO NCs without acetic acid washing.

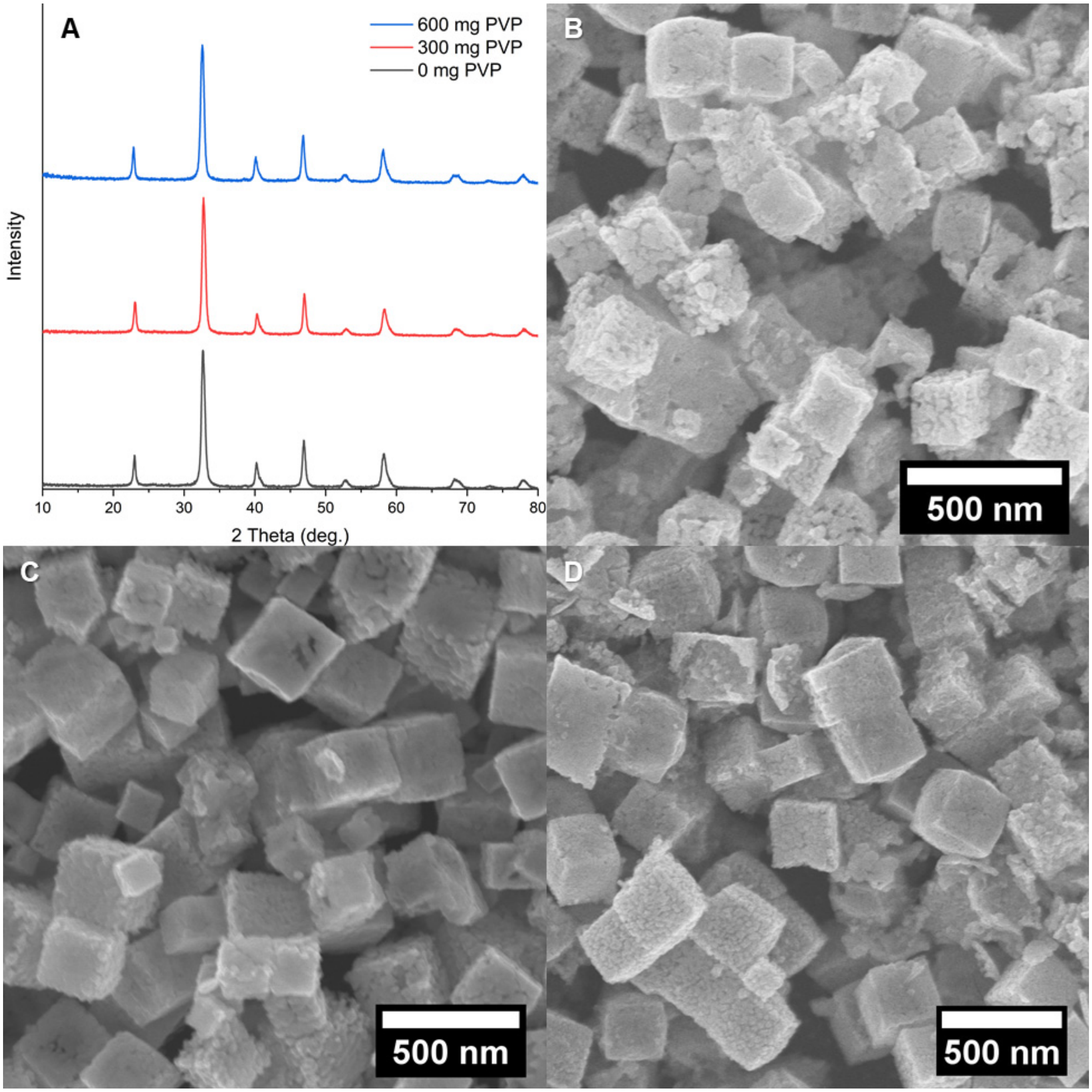

Figure S4. (A) XRD and (B-D) SEM images of LNMO NCs, synthesized with (B) 0, (C) 300, and (D) 600 mg of PVP, respectively

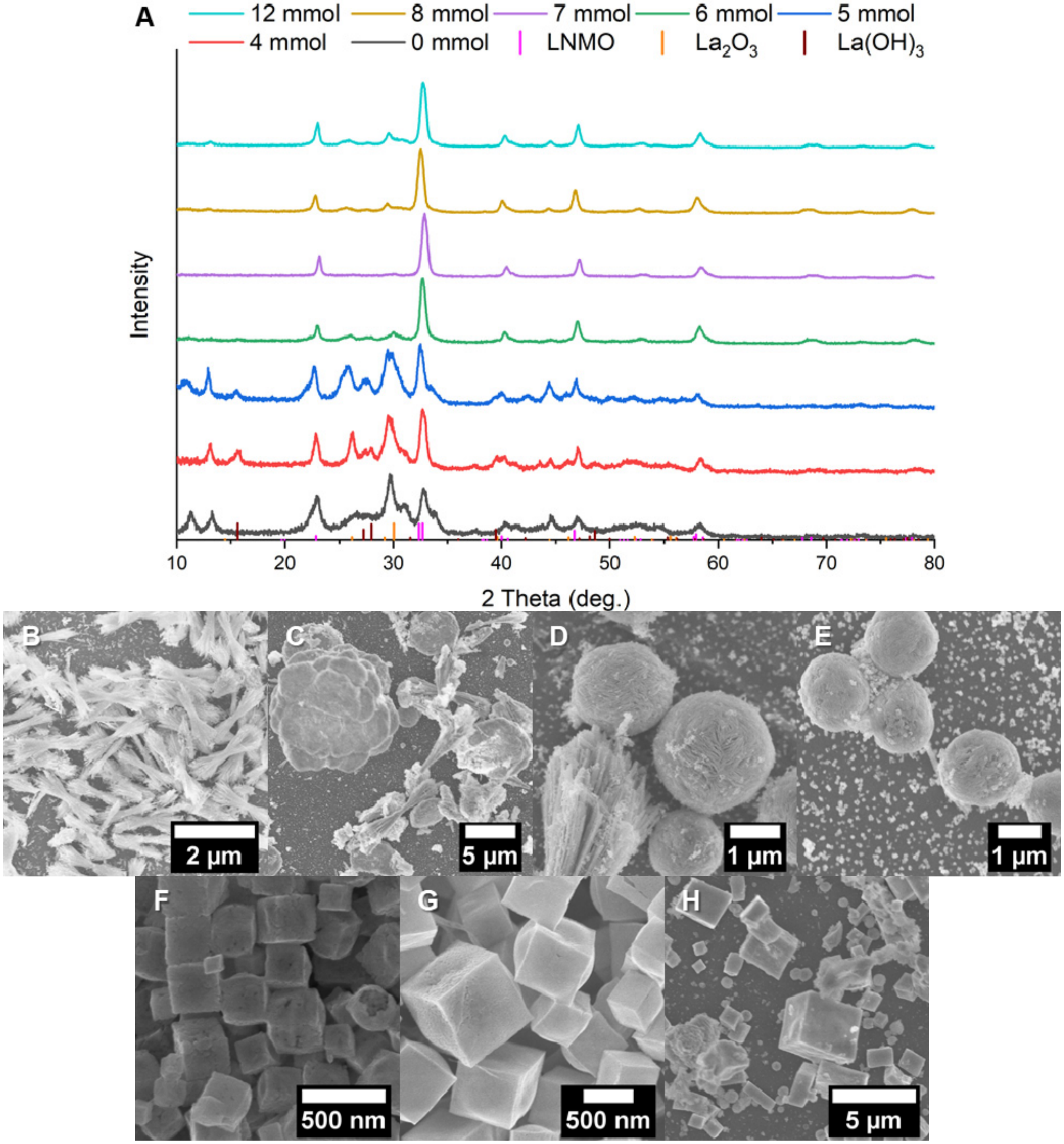

Figure S5. (A) XRD patterns and (B-H) SEM images of LNMO synthesized with (B) 0, (C) 4, (D) 5, (E) 6, (F) 7, (G) 8, and (H) 12 mmol of glycine, respectively.

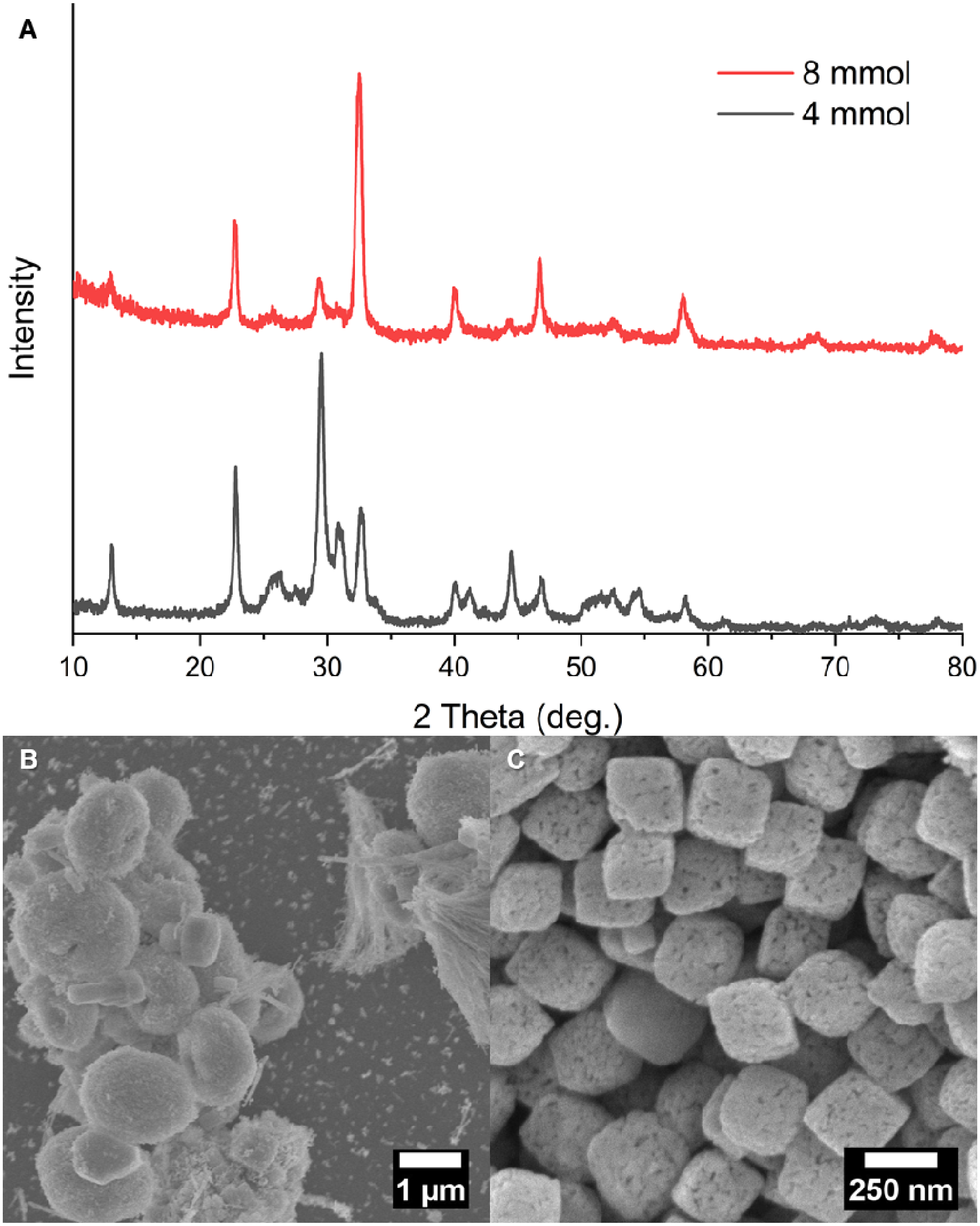

Figure S6. (A) XRD patterns and (B, C) SEM images of LMO synthesized with (B) 4 and (C) 8 mmol of glycine, respectively.

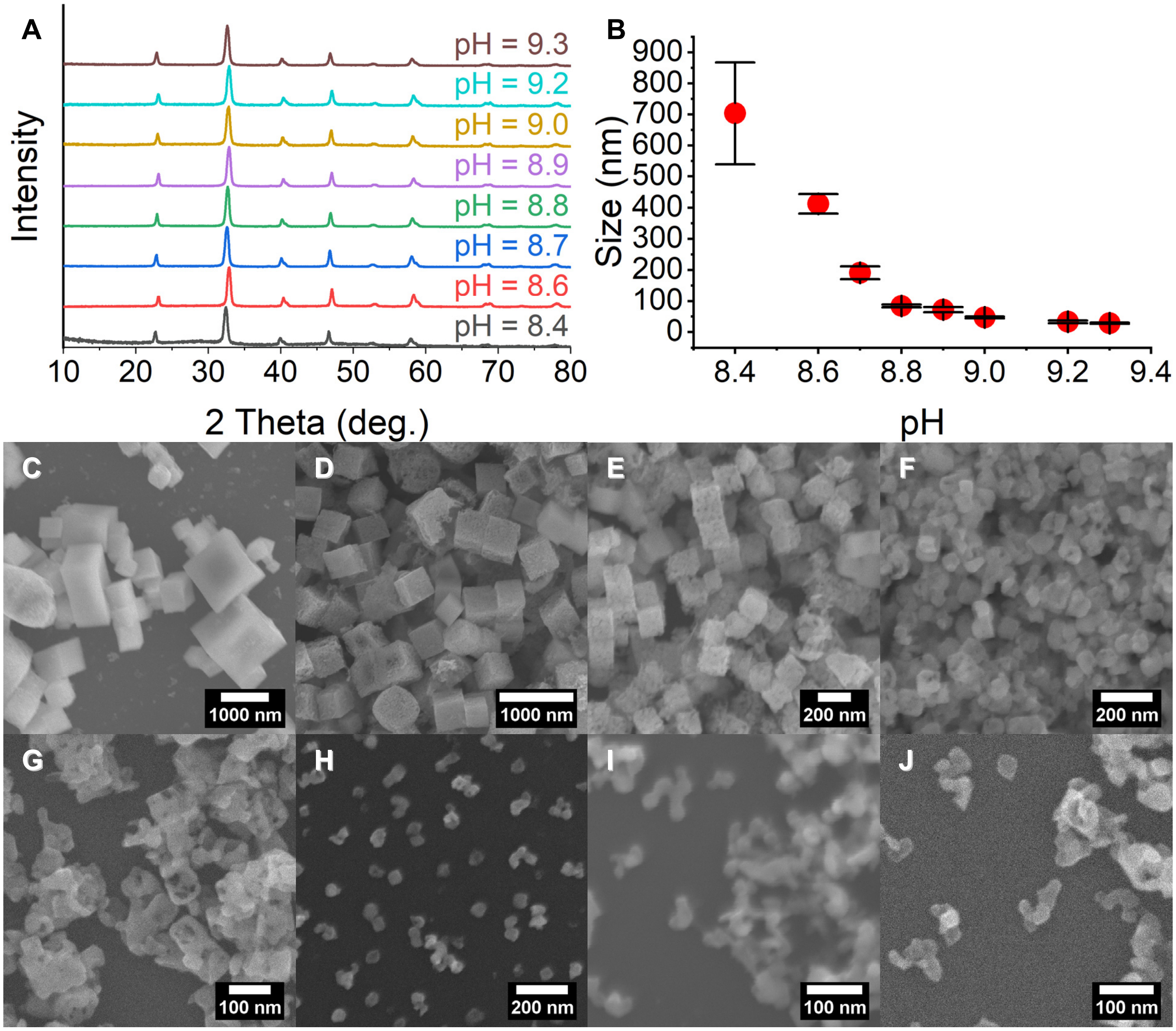

Figure S7. (A) XRD patterns. (B) Plot summarizing the effect of pH on size. (C-J) SEM images of LMO NCs, synthesized with a pH of (C) 8.4, (D) 8.6, (E) 8.7, (F) 8.8, (G) 8.9, (H) 9.0, (I) 9.2, and (J) 9.3, respectively.

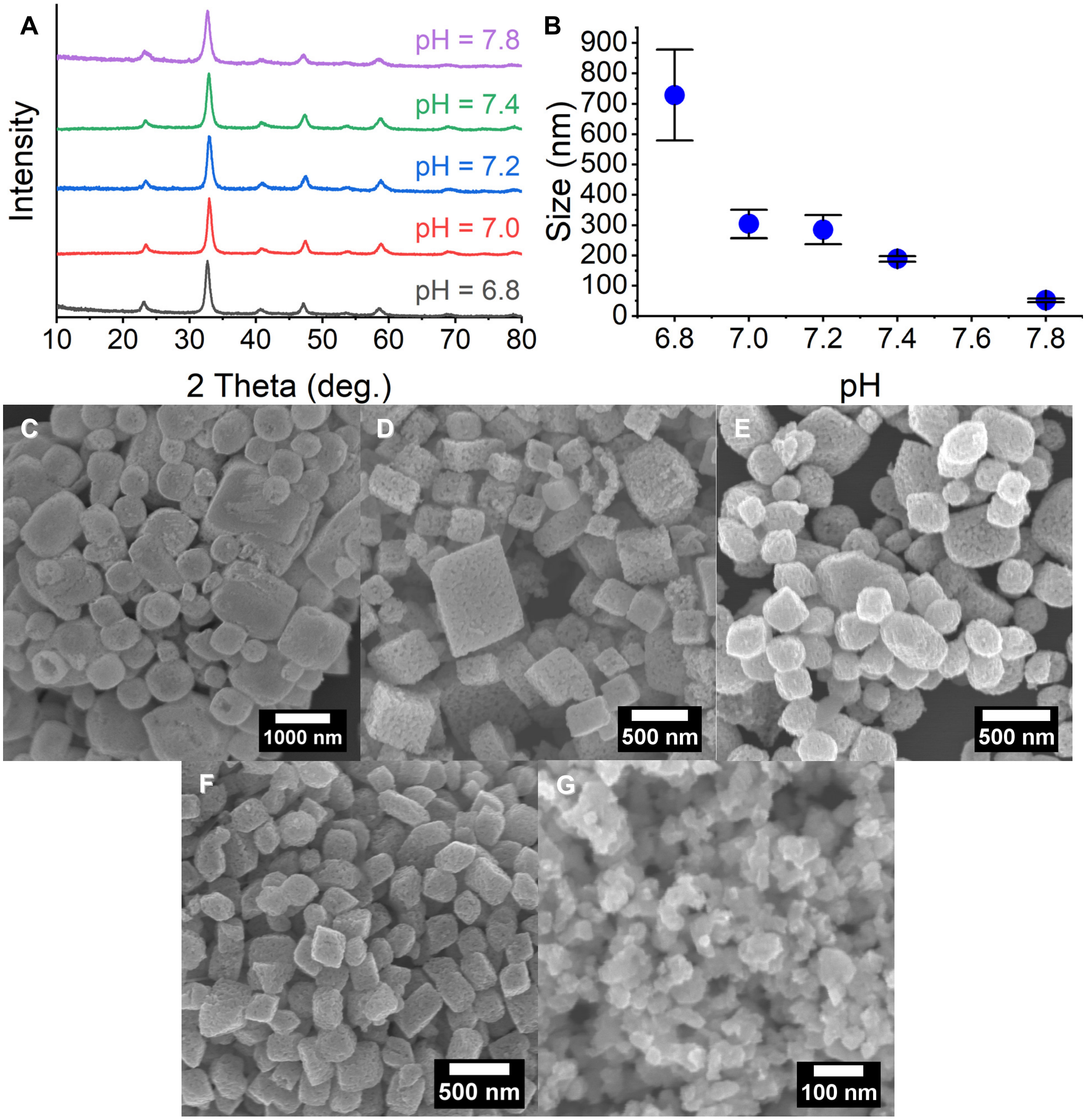

Figure S8. (A) XRD patterns. (B) Plot summarizing the effect of pH on size. (C-J) SEM images of LNO NCs, synthesized with a pH of (C) 6.8, (D) 7.0, (E) 7.2, (F) 7.4, and (G) 7.8, respectively.

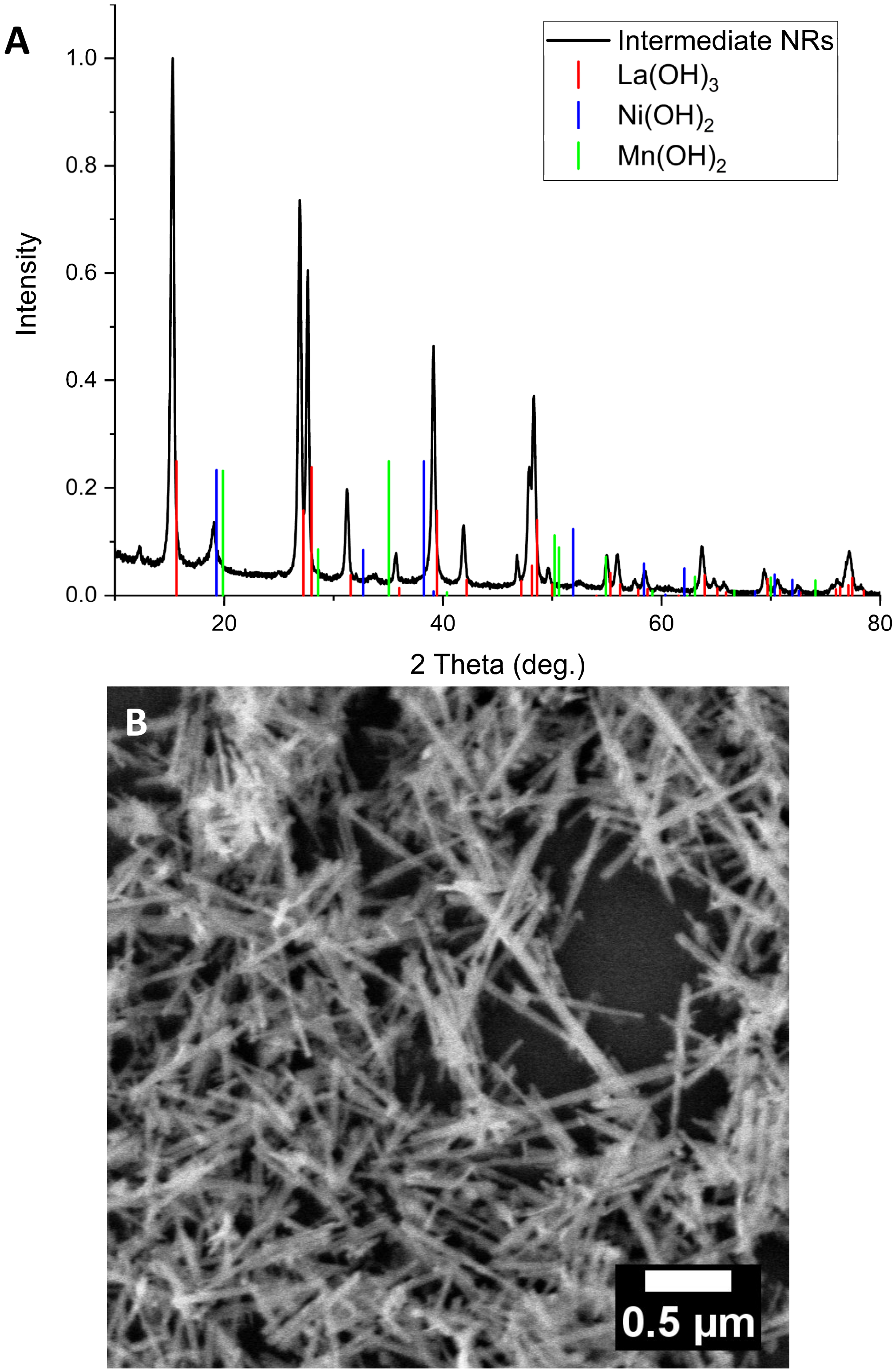

Figure S9. (A) XRD pattern and (B) SEM image of the metal hydroxide nanowire intermediate, created in the generation of LNMO

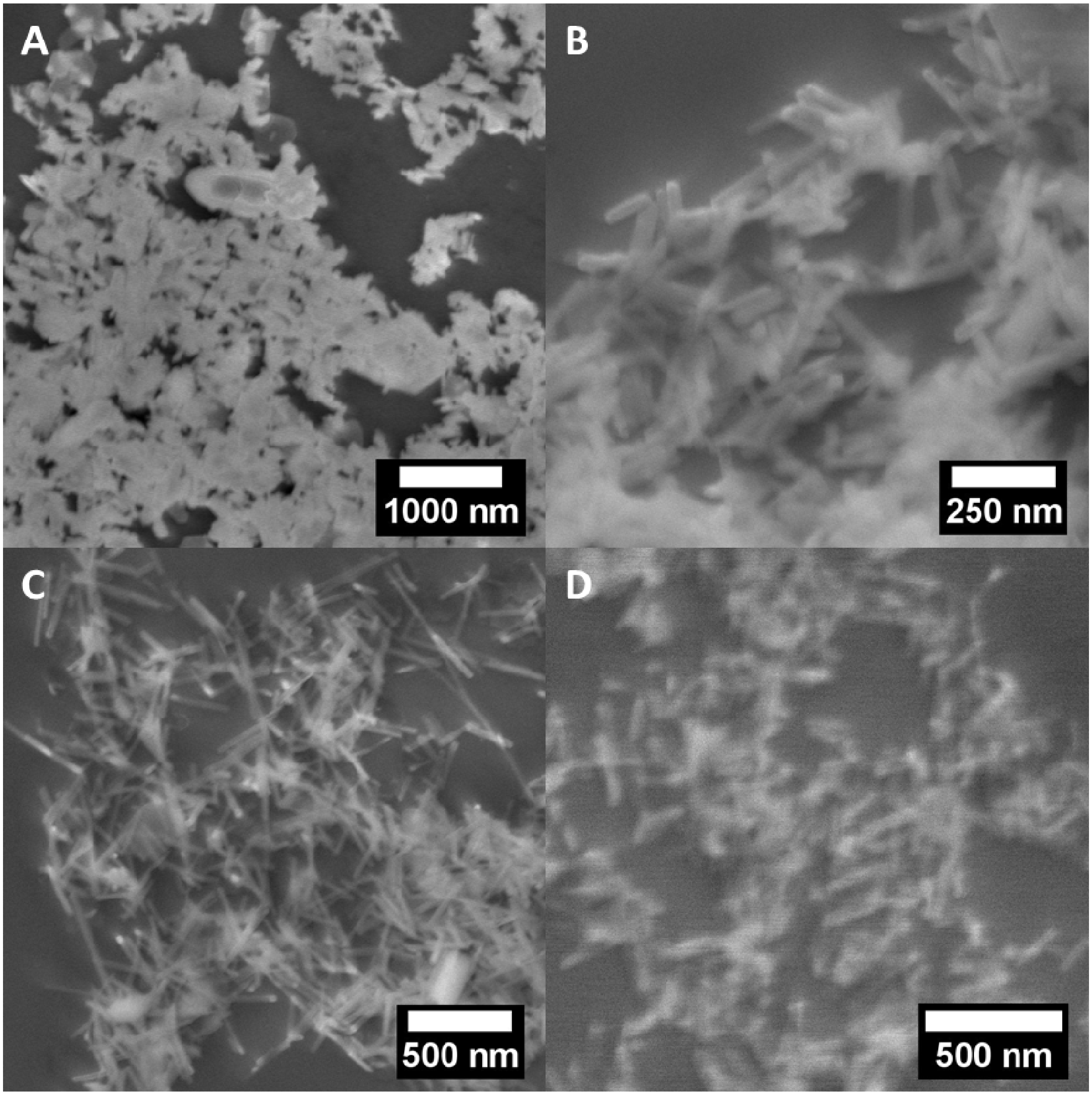

Figure S10. SEM images of intermediate nanowires, produced during the synthesis of LNMO with (A) ethanol as the solvent, (B) KCl added, (C) $KMnO_4$ as the Mn source, and (D) a hydrothermal reaction temperature of 150°C

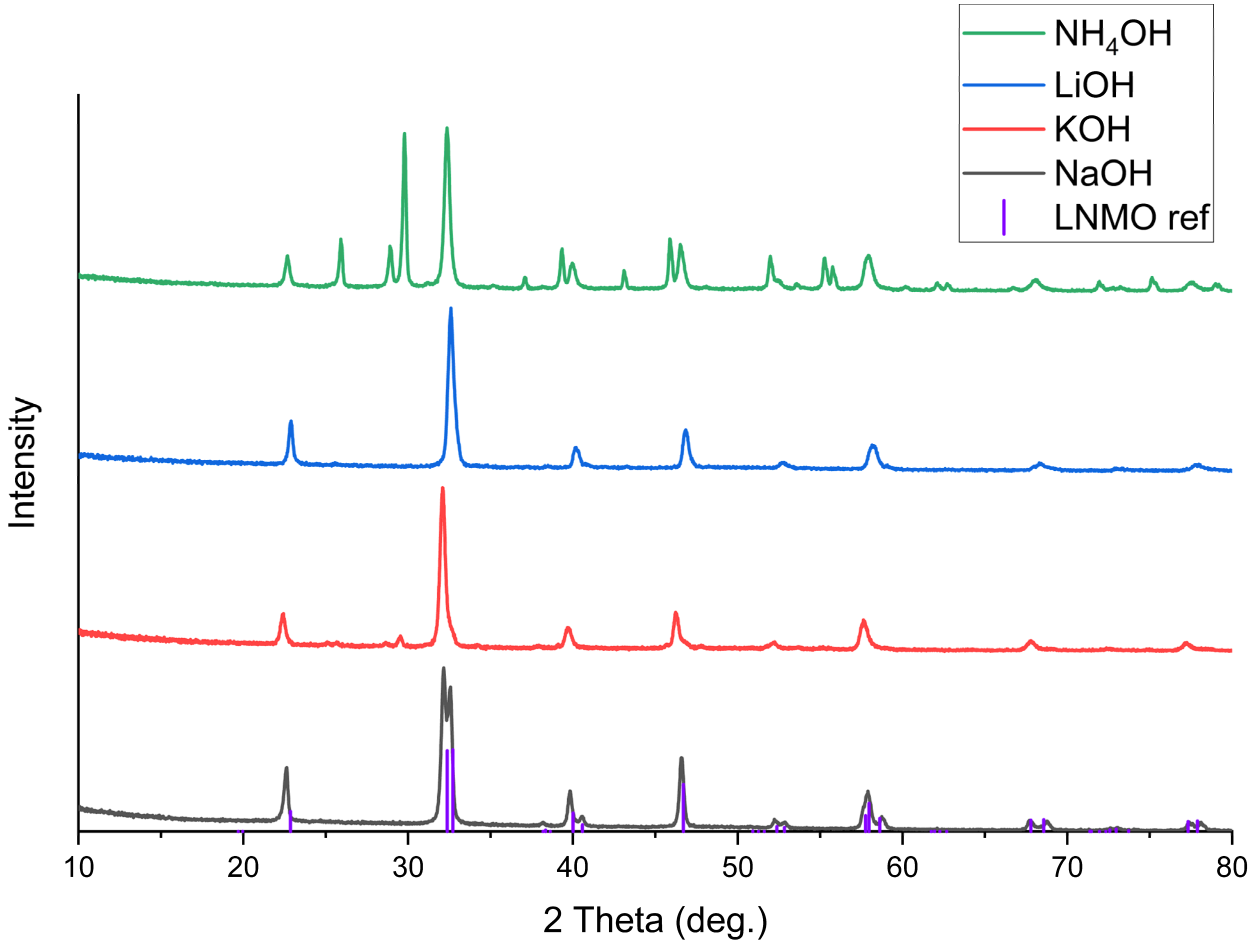

Figure S11. XRD patterns of LNMO nanorods, synthesized using NH_4OH (green), LiOH (blue), KOH (red), and NaOH (black), respectively, which were subsequently annealed at 1000°C. As a means of comparison, the LNMO reference pattern is presented (purple).[9]

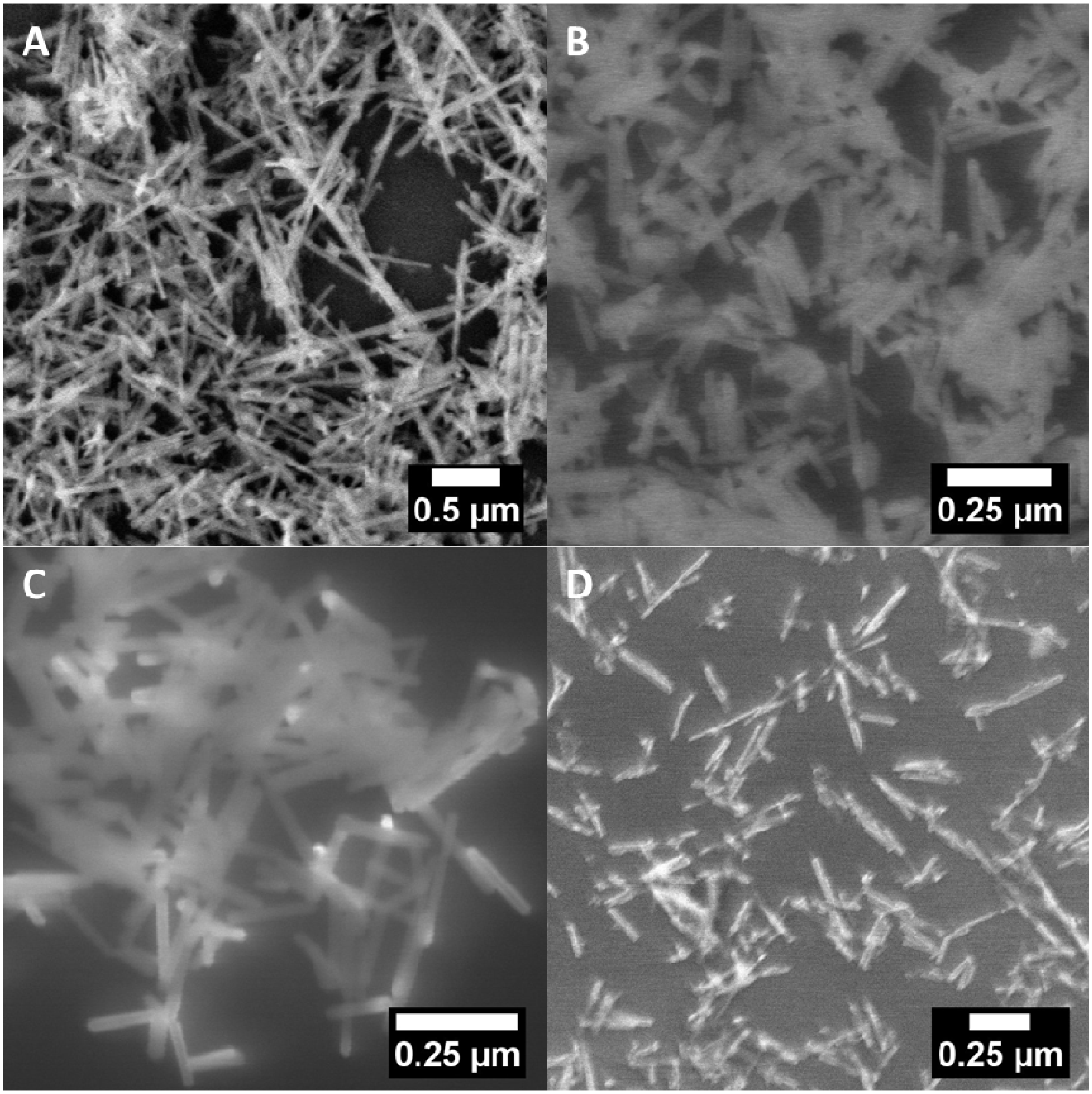

Figure S12. SEM images of the intermediate nanorods (prepared in the synthesis of LNMO), synthesized using (A) NaOH, (B) KOH, (C) LiOH, and (D) NH_4OH, respectively.

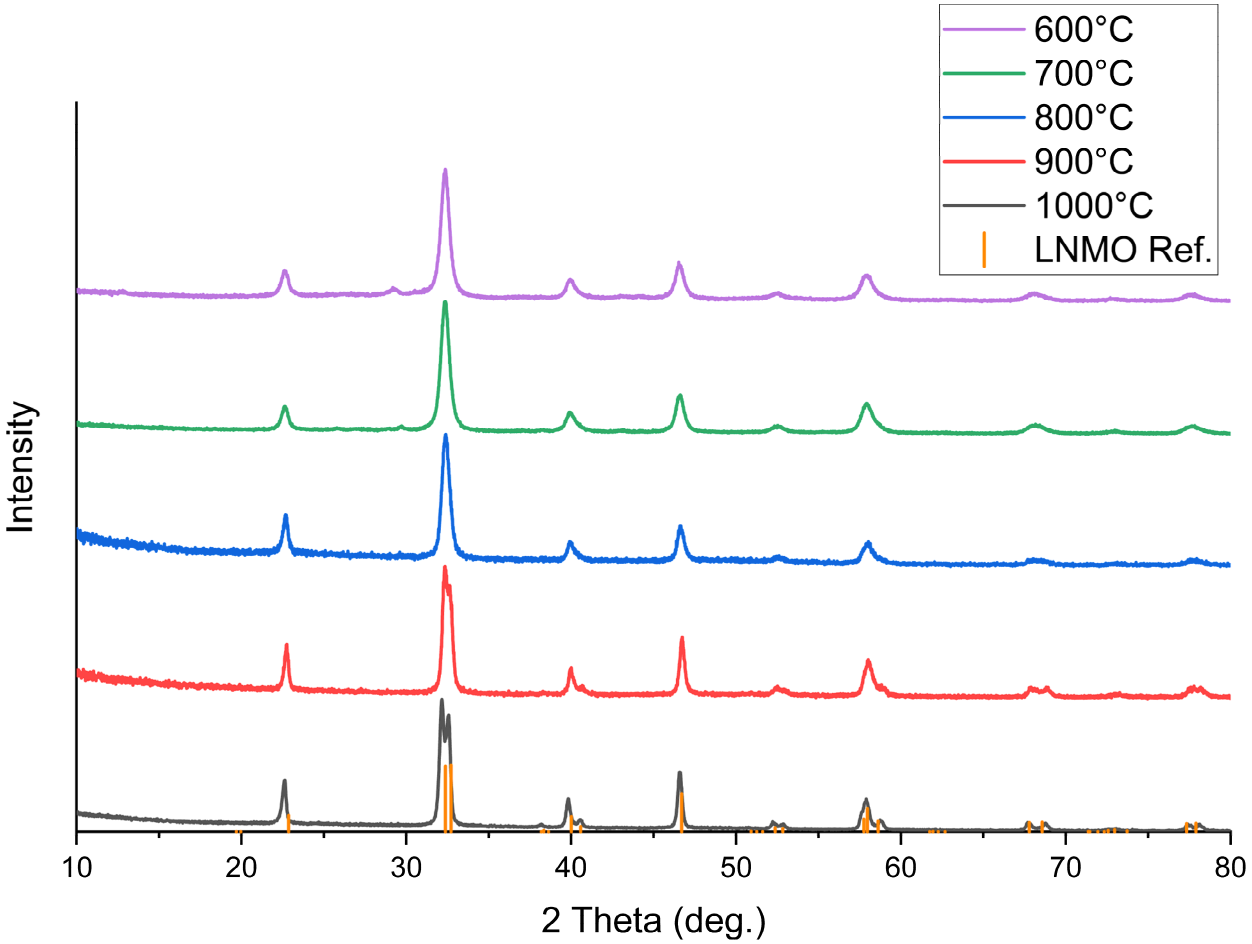

Figure S13. XRD patterns of LNMO nanorods, annealed at 600 (purple), 700 (green), 800 (blue), 900 (red), and 1000°C (black), respectively, for 1 h. The reference pattern of LNMO is shown in orange.[9]

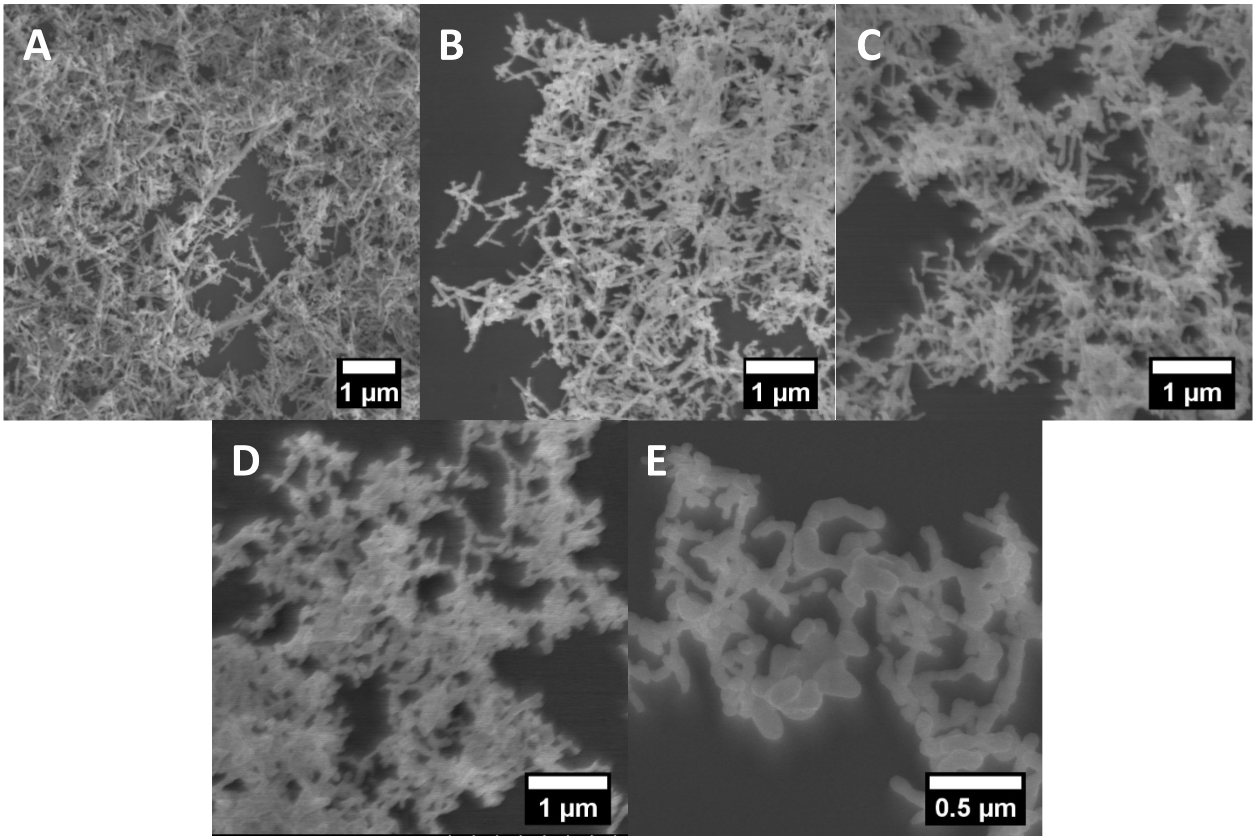

Figure S14. SEM images of LNMO nanorods, annealed at (A) 600, (B) 700, (C) 800, (D) 900, and (E) 1000°C, respectively.

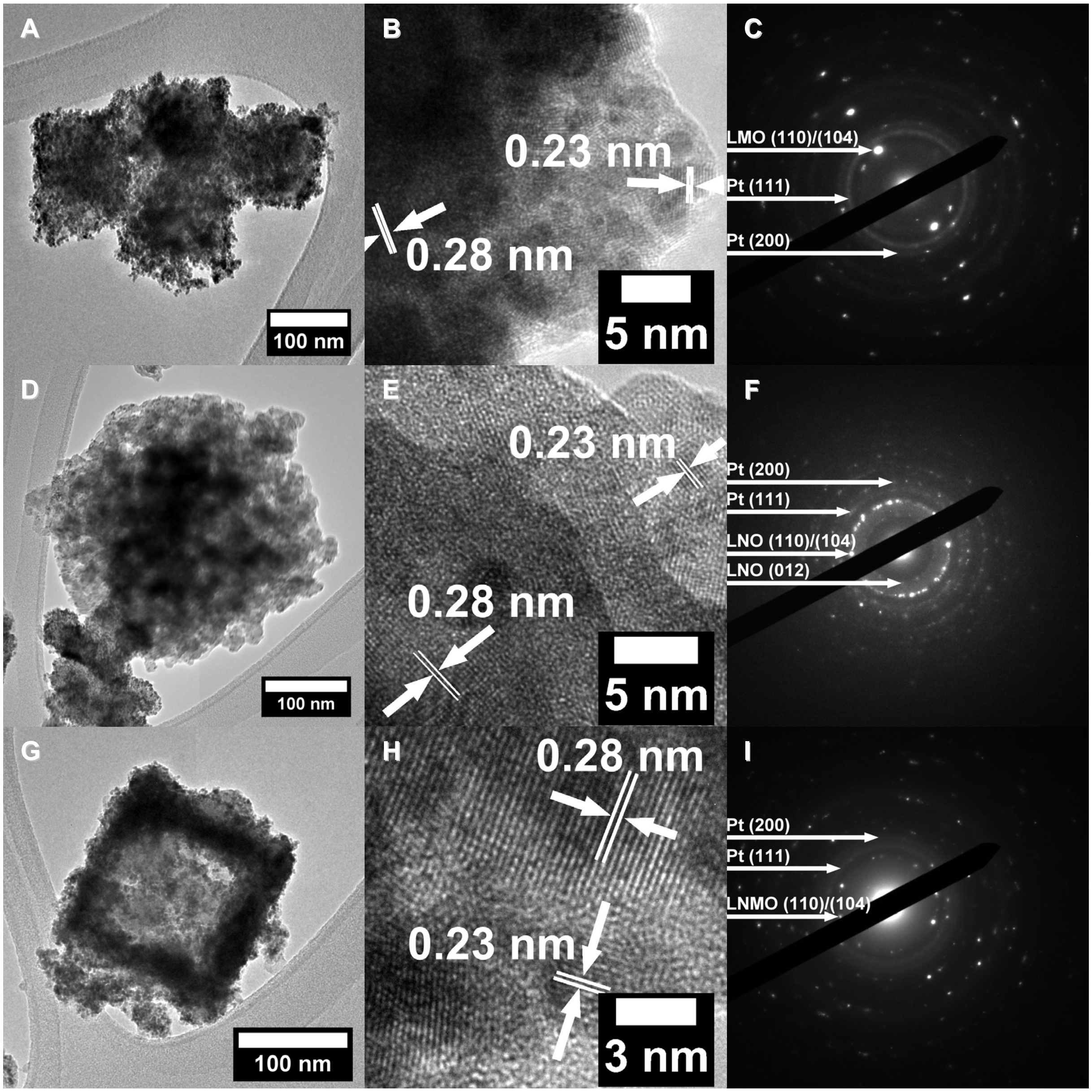

Figure S15. (A, D, G) TEM images, (B, E, H) HRTEM images with measured *d*-spacings, and (C, F, I) SAED patterns for Pt-decorated (A-C) LMO NCs, (D-F) LNO NCs, and (G-I) LNMO-8.9 NCs, respectively.

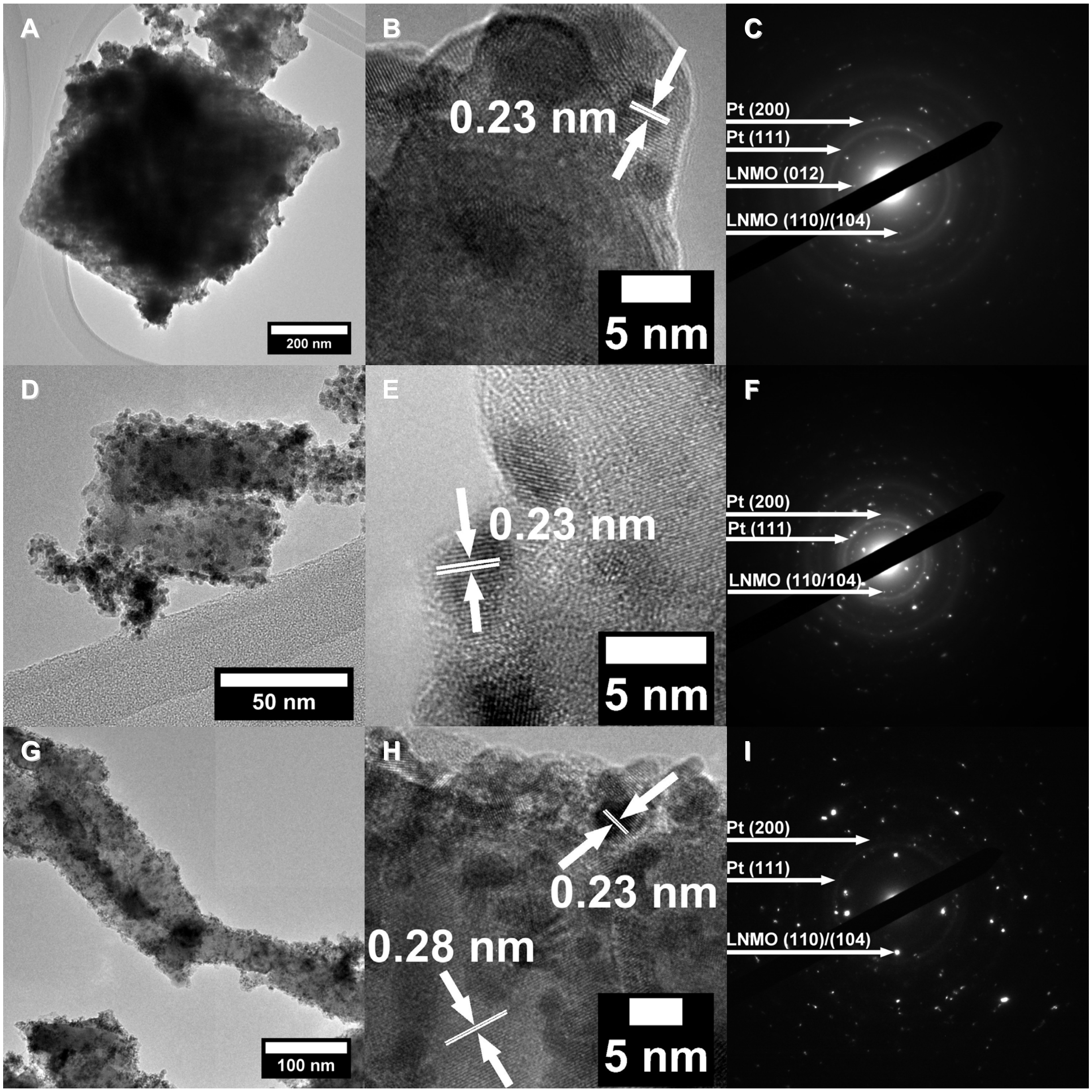

Figure S16. (A, D, G) TEM images, (B, E, H) HRTEM images with measured *d*-spacings, and (C, F, I) SAED patterns for Pt-decorated (A-C) LNMO-8.7 NCs, (D-F) LNMO-9.3 NCs, and (G-I) LNMO NRs, respectively.

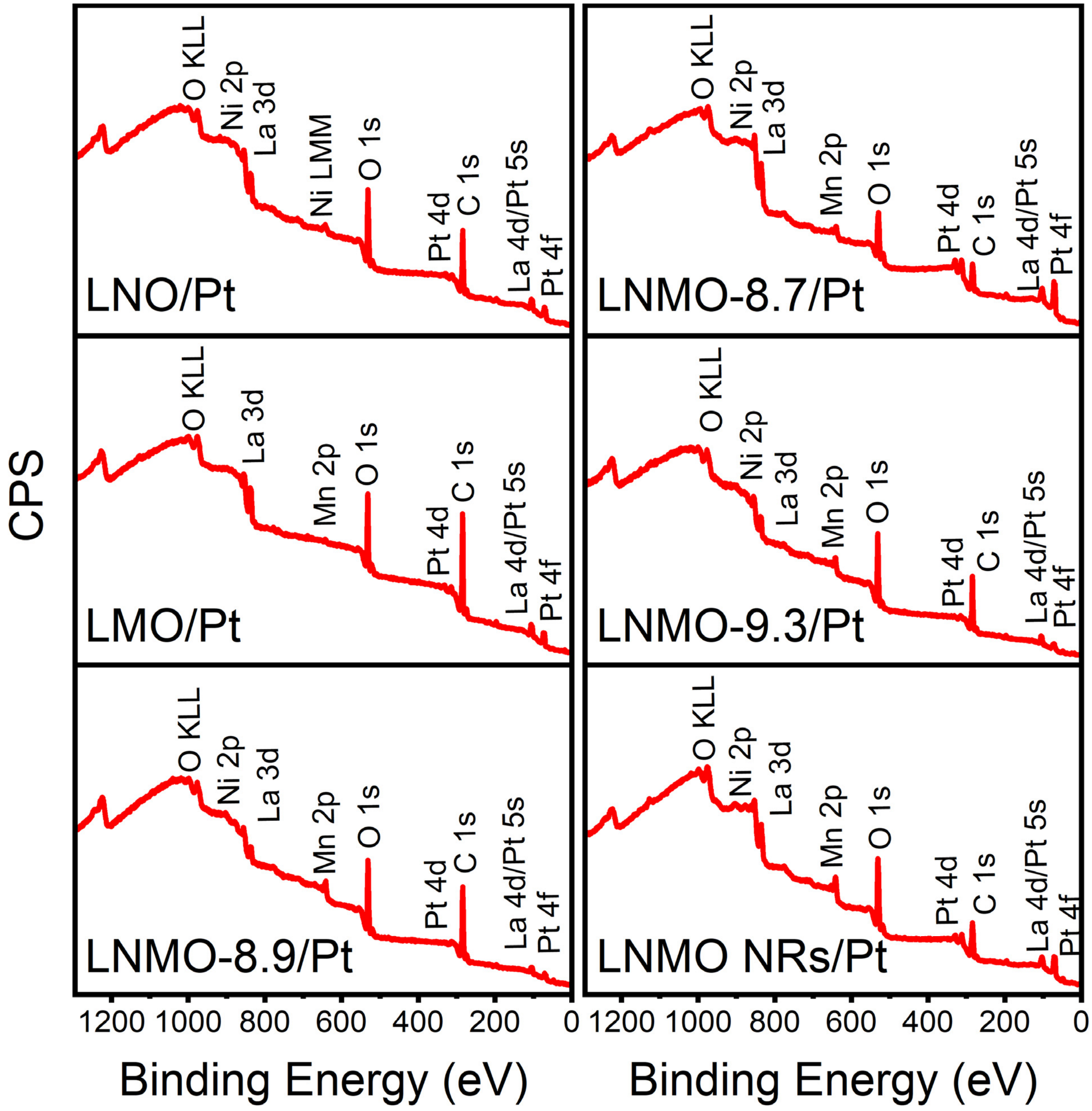

Figure S17. XPS survey spectra, corresponding to LNO/Pt, LMO/Pt, LNMO-8.9/Pt, LNMO-8.7/Pt, LNMO-9.3/Pt, and LNMO NRs/Pt, respectively.

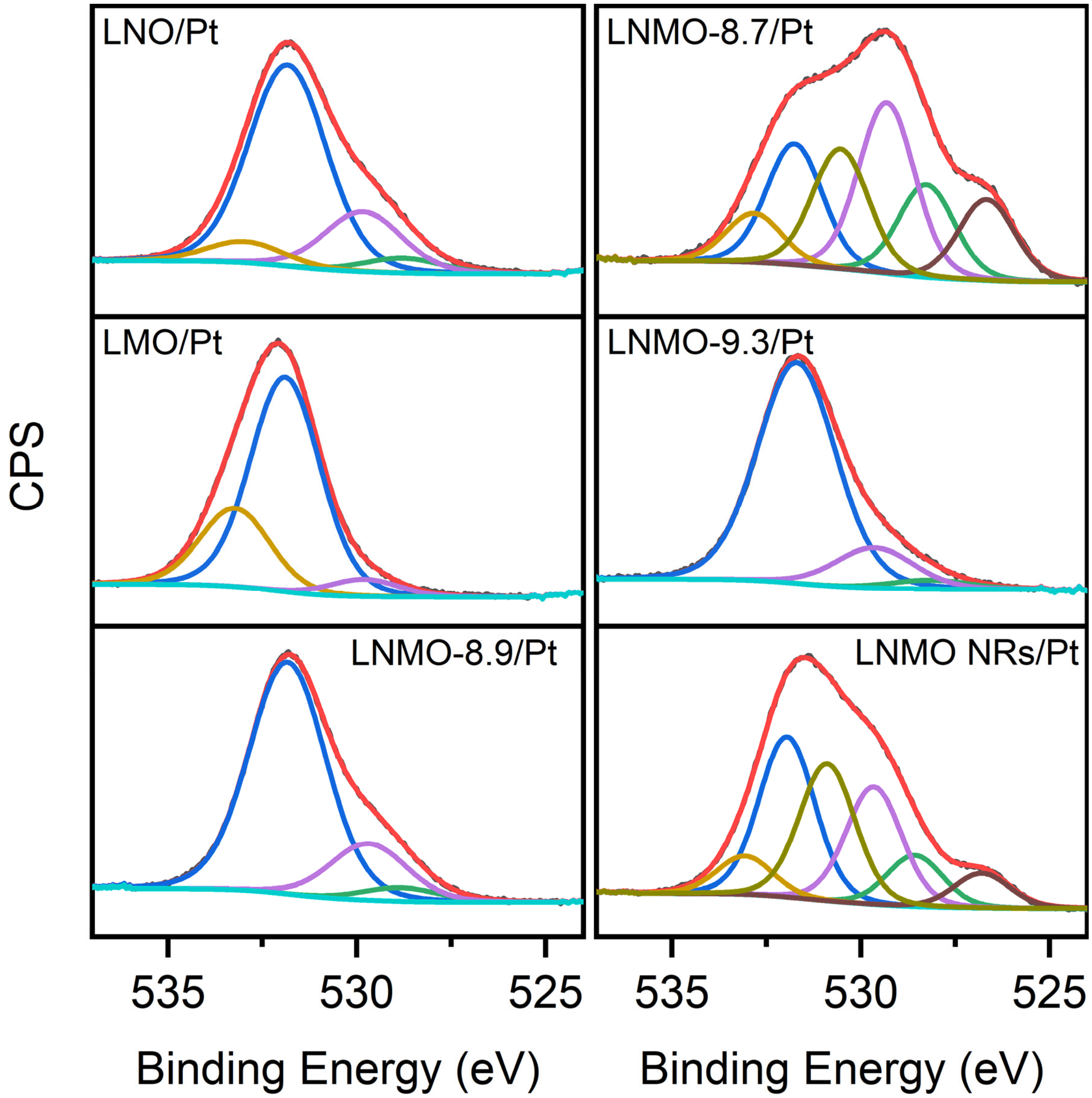

Figure S18. O 1*s* XPS spectra corresponding to LNO/Pt, LMO/Pt, LNMO-8.9/Pt, LNMO-8.7/Pt, LNMO-9.3/Pt, and LNMO NRs/Pt, respectively.

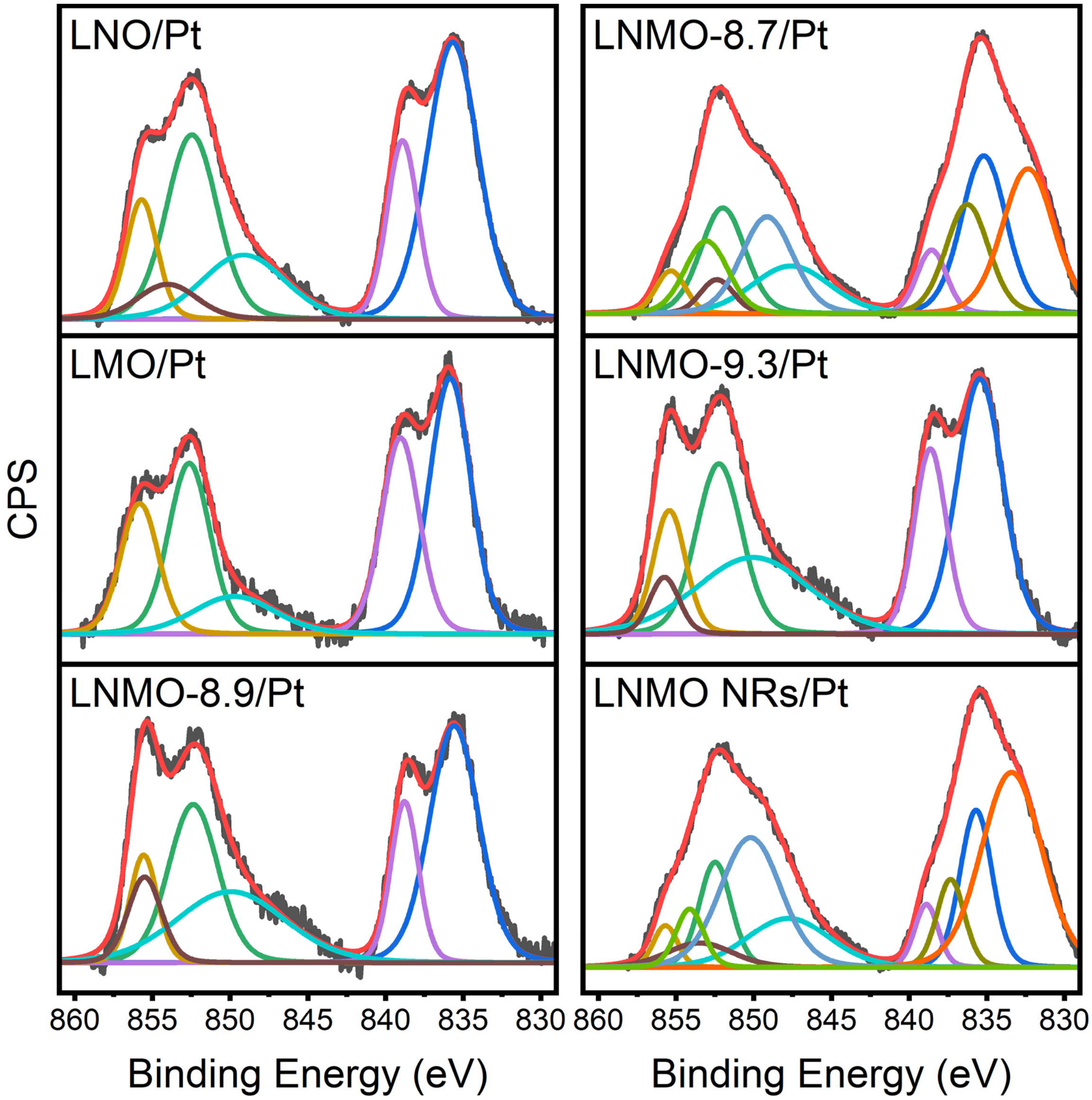

Figure S19. Background subtracted La 3*d* and Ni 2*p*$_{3/2}$ XPS spectra corresponding to LNO/Pt, LMO/Pt, LNMO-8.9/Pt, LNMO-8.7/Pt, LNMO-9.3/Pt, and LNMO NRs/Pt, respectively.

Table S1. Summary of O 1*s* XPS peak positions for the perovskite/Pt heterostructures.

Component	**LMO**	**LNO**	**LNMO-8.7**	**LNMO-8.9**	**LNMO-9.3**	**LNMO NRs**
C=O or COO^-	---	----	526.7 eV	---	---	526.8 eV
Lattice Oxygen	---	528.8 eV	528.3 eV	528.8 eV	528.1 eV	528.6 eV
Lattice Oxygen	529.8 eV	529.8 eV	529.3 eV	529.7 eV	529.6 eV	529.6 eV
O_{ads}	---	---	530.6 eV	---	---	530.9 eV
OH	531.9 eV	531.8 eV	531.8 eV	531.8 eV	531.7 eV	531.9 eV
H_2O	533.2 eV	533.0 eV	532.9 eV	---	---	533.1 eV

Table S2. Summary of XPS results for the perovskite/Pt heterostructures within the La 3*d* and Ni 2$p_{3/2}$ regions, respectively.

Component	**LMO**	**LNO**	**LNMO-8.7**	**LNMO-8.9**	**LNMO-9.3**	**LNMO NRs**
La 3$d_{5/2}$ (La_2O_3)	---	---	832.34 eV	---	---	833.4 eV
La 3$d_{5/2}$ ($La(OH)_3$)	835.8 eV	835.7 eV	835.2 eV	835.6 eV	835.4 eV	835.7 eV
La 3$d_{5/2}$ Satellite (La_2O_3)	---	---	836.3 eV	---	---	837.3 eV
La 3$d_{5/2}$ Satellite ($La(OH)_3$)	839.0 eV	838.9 eV	838.5 eV	838.8 eV	838.6 eV	838.9 eV
Plasmon	849.7 eV	849.1 eV	847.6 eV	850.0 eV	850.1 eV	847.8 eV
La 3$d_{3/2}$ (La_2O_3)	---	---	849.1 eV	---	---	850.2 eV
La 3$d_{3/2}$ ($La(OH)_3$)	852.6 eV	852.5 eV	852.0 eV	852.4 eV	852.2 eV	852.5 eV
La 3$d_{3/2}$ Satellite (La_2O_3)	---	---	853.1 eV	----	---	854.1 eV

Ni 2*p*$_{3/2}$	---	854.0 eV	852.4 eV	855.5 eV	855.8 eV	853.5 eV
La 3*d*$_{3/2}$ Satellite (La(OH)$_3$)	855.8 eV	855.7 eV	855.3 eV	855.6 eV	855.4 eV	855.7 eV

References

1. Alam, M.; Karmakar, K.; Pal, M.; Mandal, K., Electrochemical supercapacitor based on double perovskite Y_2NiMnO_6 nanowires. *RSC Adv.* **2016,** *6* (115), 114722-114726.
2. Kitadai, N., Dissolved Divalent Metal and pH Effects on Amino Acid Polymerization: A Thermodynamic Evaluation. *Orig. Life Evol. Biosph.* **2017,** *47* (1), 13-37.
3. Yamabe, S.; Ono, N.; Tsuchida, N., Molecular Interactions between Glycine and H_2O Affording the Zwitterion. *J. Phys. Chem. A* **2003,** *107* (39), 7915-7922.
4. Tanaka, Y.; Saito, H.; Tsutsumi, Y.; Doi, H.; Nomura, N.; Imai, H.; Hanawa, T., Effect of pH on the interaction between zwitterions and titanium oxide. *J. Colloid and Interface Sci.* **2009,** *330* (1), 138-143.
5. Haynes, W. M., *CRC Handbook of Chemistry and Physics*. CRC Press: 2016.
6. Feng, J.; Li, X.; Wang, M.; Zheng, X.; Bai, J.; Wang, L.; Peng, Y., One-pot, template-free synthesis of hydrophobic single-crystalline $La(OH)_3$ nanowires with tunable size and their d0 ferromagnetic properties. *RSC Adv.* **2015,** *5* (21), 16093-16100.
7. Wang, Y.; Fan, H. J., Improved thermoelectric properties of $La_{1-x}Sr_xCoO_3$ nanowires. *J. Phys. Chem. C* **2010,** *114* (32), 13947-13953.
8. Hirosaki, N.; Ogata, S.; Kocer, C., Ab initio calculation of the crystal structure of the lanthanide Ln_2O_3 sesquioxides. *J. Alloys Compd.* **2003,** *351* (1), 31-34.
9. Bull, C. L.; Gleeson, D.; Knight, K. S., Determination of B-site ordering and structural transformations in the mixed transition metal perovskites La_2CoMnO_6 and La_2NiMnO_6. *J. Phys. Condens. Matter* **2003,** *15* (29), 4927-4936.